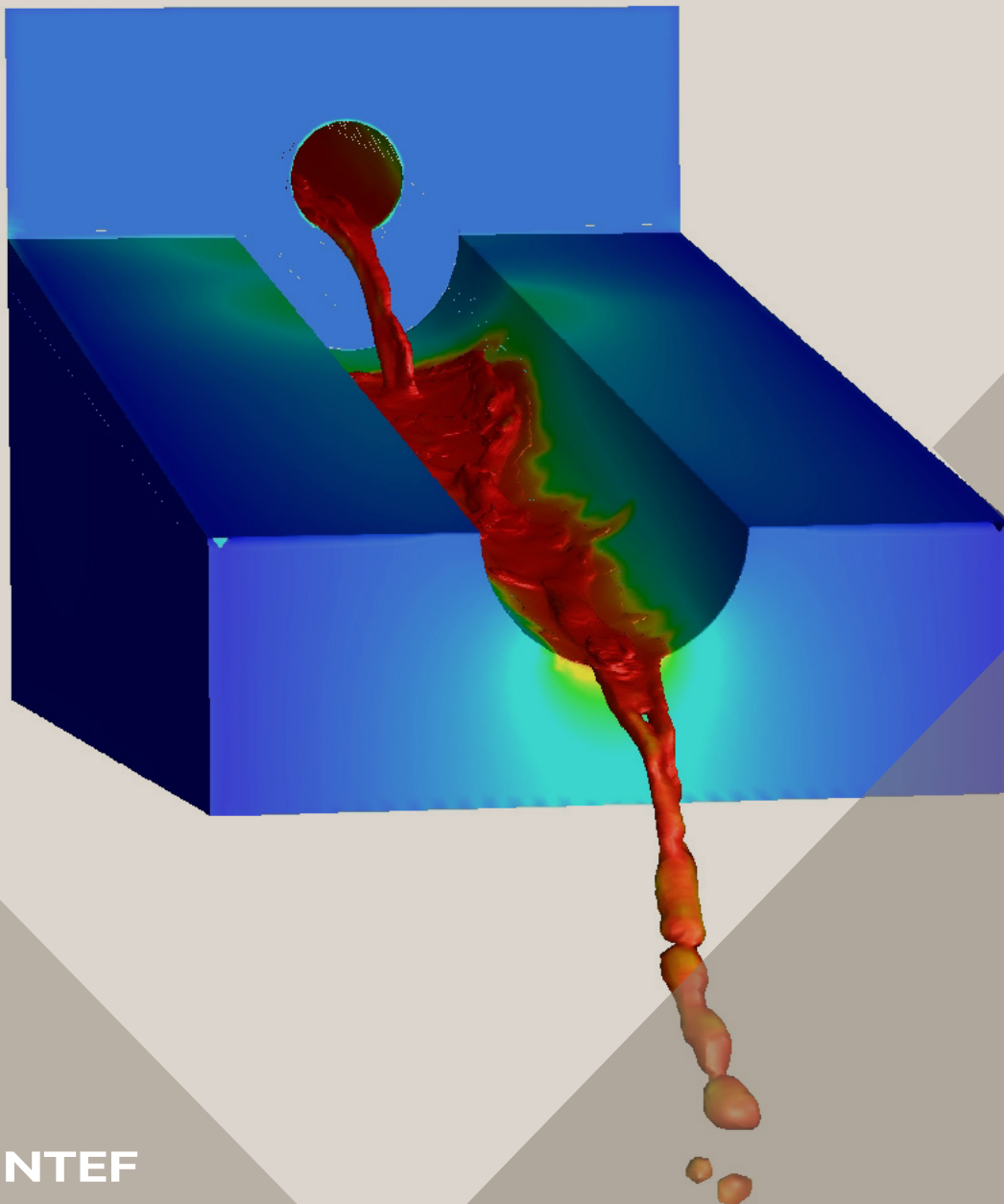14th International Conference on CFD in
Oil & Gas, Metallurgical and Process Industries
SINTEF, Trondheim, Norway, October 12–14, 2020

Proceedings from the 14th International Conference on CFD in Oil & Gas, Metallurgical and Process Industries

SINTEF

SINTEF Proceedings

Editors:
Jan Erik Olsen, Jan Hendrik Cloete and Stein Tore Johansen

Proceedings from the 14th International Conference on CFD in Oil & Gas, Metallurgical and Process Industries

SINTEF, Trondheim, Norway
October 12–14, 2020

SINTEF Academic Press

MODELLING OF MASS TRANSFER IN A STEELMAKING LADLE

Nelson JOUBERT[1,2]*, **Pascal GARDIN**[1]†, **Stéphane ZALESKI**[2]‡, **Stéphane POPINET**[2]·

[1]ArcelorMittal Maizières Research, BP 30320, Voie Romaine, 57283

Maizières-lès-Metz Cedex, FRANCE

[2]Sorbonne Université, CNRS, UMR 7190, Institut Jean Le Rond d'Alembert,

BP 162, 4, Place Jussieu, 75252 Paris Cedex 05, FRANCE

* E-mail : nelson.joubert@sorbonne-universite.fr
† E-mail : pascal.gardin@arcelormittal.com
‡ E-mail : stephane.zaleski@sorbonne-universite.fr
· E-mail : stephane.popinet@sorbonne-universite.fr

ABSTRACT

Mass transfer between liquid steel and slag is an important point during secondary metallurgy for prediction of the chemical reaction rate and adjustment of liquid steel composition. We want to study this phenomenon in the case of an argon gas bottom blown ladle. To do so we use an experimental and numerical water model at ambient temperature. We measure experimentally the mass transfer of thymol between water and oil when the air flow rate injected is varied. The experimental results show that two mass transfer regimes can be observed. The mass transfer regime change could be correlated to the continuous formation of oil droplets in the water when the air flow rate is above a critical value. The numerical results represent qualitatively well the fluid flow of the water model. But the numerical results cannot reproduce different mass transfer regimes as observed experimentally and, have a tendency to overestimate the mass transfer.

Keywords: CFD, hydrodynamics, multiphase flow, mass transfer.

NOMENCLATURE

Greek Symbols

ρ Mass density, [kg/m^3].
μ Dynamic viscosity, [kg/m.s].
ν Kinematic viscosity, [m²/s].
δ Boundary layer thickness, [m].
σ Surface tension, [N/m].
χ Volume fraction, [-].
ϵ Rate of dissipation of turbulence kinetic energy, [m²/s].
η Kolmogorov length scale, [m].
λ_B Batchelor length scale, [m].

Latin Symbols

L Width of the ladle, [m].
h Height, [m].
d Diameter, [m].
V Volume, [l].
Q Gas flow rate, [l/min].
g Gravitational acceleration, [m/s^2].
J Mass flux, [kg/m^{2}s].

A Interfacial area, [m^2].
C Concentration, [g/l].
D Diffusion coefficient, [m²/s].
k Mass transfer coefficient, [m/s].
p Pressure, [Pa].
u Velocity, [m/s].
T Numerical tracer concentration, [g/l].
P Partition coefficient, [-].
N Maximum number of grid points in one direction [-].
Fr Froude number, [-].
Sc Schmidt number, [-].
Sh Sherwood number, [-].

Sub/superscripts

a Air.
w Water.
o Oil.
c Concentration.
0 Initial condition.
th Thymol.
$'$ Interface value.
ov Overall.
inj Injector.
il Industrial ladle.
ml Model ladle.
$norm$ Normalized value.
$^-$ Time average.
∞ Fluid bulk.

INTRODUCTION

In numerous natural and industrial processes, chemical reaction occurs together with a fluid flow and possibly other physical phenomena. In the steel industry, during the secondary metallurgy step, the adjustment of liquid steel composition at high temperature in a ladle involves several chemical reactions between steel and slag (another liquid phase of variable chemical composition depending on the expected chemical reaction with steel) (Riboud & Vasse, 1985). Chemical reactions can be

broken down into three stages: transport by convection of reactive species within the liquid phase toward the interface, transport by molecular diffusion through concentration boundary layer and finally chemical reaction at the interface. The global kinetics is governed by the kinetics of the slowest stage. In the case of a chemical reaction between liquid steel and slag, it is generally accepted that chemical reactions at the interface are very fast. Then, the steps governing the global kinetics are the convective and diffusive transport or mass transfer of reactive species. Therefore, we want especially to characterise the mass transfer of reactive species between the liquid steel and slag phase. Here, for example, the process we are interested in to reproduce is the desulfurization of liquid steel by chemical reaction with slag under argon gas bubbling. Previous studies attempted to model experimentally the process either with a cold model (Kim & Fruehan, 1987; Ishida et al., 1981; Mietz & Oeters, 1991; Wei & Oeters, 1992) or a high-temperature model (Hirasawa et al., 1987a; Hirasawa et al., 1987b). Other studies try to model the process numerically (Lou & Zhu, 2014; Lou & Zhu, 2015). The results showed some change in the mass transfer regime between the two phases when the gas flow rate reaches a particular value. From the studies in the literature several explanations are made to explain the observed mass transfer regime change:

- Change of the steel phase flow behaviour;
- Change of the slag phase flow behaviour;
- Increase of steel-slag exchange area.

This could also be a combination of the three assumptions. But in the literature, it is generally acknowledged that the observed mass transfer regime change is due to the high deformation of the slag layer leading possibly to its fragmentation into droplet in liquid steel (Calabrese et al., 1986; Iguchi et al., 1994; Xiao et al., 1987). Slag droplets formation would increase the exchange area between the two phases. In order to verify this assumption and the mass transfer regime change, we build an experimental water model of the process with its numerical model. We will detail in the following the results obtained experimentally and numerically on the mass transfer characterization.

MODEL DESCRIPTION

We want to establish a model that allows to reproduce the main flow characteristics that can be observed in an industrial ladle especially when the gas flow rate is changed and with the easiest experimental setup as possible.

EXPERIMENTAL MODEL

The main characteristics of the flow consist of a gas bubble plume, and the water-oil layer interaction. Because in this study the gas bubble plume is mostly used to generates agitation of the liquid phase, we will not focus on the gas bubble plume. Nevertheless, the gas flow rate remains an important parameter as it will globally put in motion the fluids. Given the numbers of parameters of the physical model, many dimensionless number quantities can be established. As a result, the

choice of similitude to follow is not trivial and depends on the phenomena of interest. In this study, we are interested in the mass transfer characterization between liquid steel and slag. Nevertheless, this mass transfer depends strongly on the fluid flow characteristics. So, in order to reproduce the mass transfer configuration of an industrial ladle, we proceed as in Kim & Fruehan (1987) for the choice of fluids and chemical tracers that will be detailed below. Furthermore, the gas flow rate is a control parameter of the process then it will be used to reproduce the fluid flow with a scaled model of an industrial ladle. So, we proceed again as in Kim & Fruehan (1987) and we choose to follow a similitude based on the Froude number:

$$Fr = \frac{Q}{\sqrt{gh_w^5}} \qquad (1)$$

To determine the correspondence between a 200-ton industrial ladle and our model ladle gas flow rate a Fr similitude is used, and we can write:

$$Q_{il} = \lambda^{\frac{5}{2}} Q_{ml} \qquad (2)$$

The geometric scale is given by $\lambda = h_{w,il}/h_{w,ml}$ is equal to $\lambda = 1/16.6$.

In this study, we use a cubic water model of length L_x with a water and oil bath height respectively h_w and h_o at ambient temperature based on the one used by Kim & Fruehan (1987). Figure 1 displays a sketch of the experimental setup of the water model and the main geometric parameters of the ladle can be found in Table 1. It is a square section transparent ladle made with acrylic glass, with a single bottom centred circular air injection hole. The ladle is partially filled with water and a layer of oil is floating on top of the water. Air flow within the range of $[0.6 L/min : 8 L/min]$ is injected from a compressed air network and can be varied through an automate controlling the valve opening.
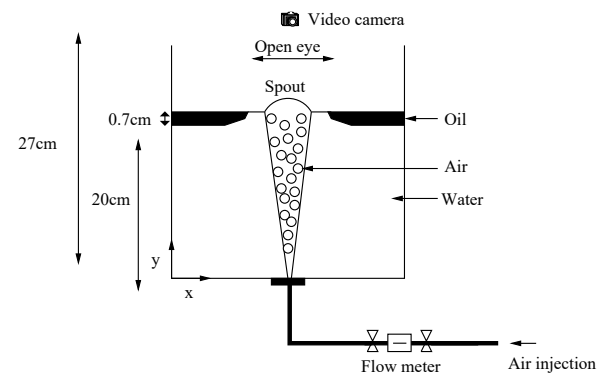
Figure 1: Schematic of the experimental setup of the water model

L	d_{inj}	h_w	h_o	V_w	V_o	h_w/L_x
0.27	$2.5 \cdot 10^{-3}$ to $7.9 \cdot 10^{-3}$	0.2	$7.0 \cdot 10^{-3}$	14.6	0.49	0.7

Table 1: Main geometrical parameters of the model

As in the industrial process, it is a three-phase model where the air phase represents the argon gas, water

represents the liquid steel, and the oil mixture layer represents the liquid slag. The choice of fluids follows the one used in Kim & Fruehan (1987) and allows us to study both hydrodynamics and mass transfer with the same fluids. The choice of water can be justified because of its kinematic viscosity $\nu_w = 1.10^{-6}\ m^2.s^{-1}$ which is very close to that of liquid steel $\nu_{steel} = 7.10^{-7}\ m^2.s^{-1}$. The oil phase is a 50-50% in volume mixture of cottonseed oil and paraffin oil. All the fluids physical parameters can be found in Table 2.

	ρ	μ	$\sigma_{a/w}$	$\sigma_{w/o}$	$\sigma_{o/a}$
Air	1.225	$1.85.10^{-5}$	$7.20.10^{-2}$		
Water	998	$1.00.10^{-3}$		$2.55.10^{-2}$	
Oil mixture	920	$7.9.10^{-2}$			$3.17.10^{-2}$

Table 2: Physical properties of fluids used in the water model

In the case of two immiscible liquids at steady-state condition, boundary layers offering resistance to the overall mass transfer are considered for both liquids. The overall mass transfer coefficient at the interface can be computed by equating mass fluxes computed using fluid film approximation of the first law of Fick:

$$J = k_w(C_w - C'_w)$$
$$-J = -k_o(C_o - C'_o) \qquad (3)$$

where $k_w = D_w/\delta_c$ and $k_o = D_o/\delta_c$. At the interface, when the concentration is at chemical equilibrium there is a discontinuity because of chemical tracer solubility difference between the two phases. It can be described by the partition coefficient:

$$P = \frac{C'_o}{C'_w} \qquad (4)$$

Combining the above equations, we can write the following mass flux equations for the water phase:

$$J = k_{ov}\left(C_w - \frac{C_o}{P}\right) \qquad (5)$$

where $k_{ov} = 1/(1/k_w + 1/Pk_o)$, and $1/k_w$, $1/Pk_o$ represent the water and oil phase mass transfer resistance. Depending on the value of Pk_o the mass transfer resistance value can be preponderant in either one of the phases or of equal importance in both phases. In the mentioned literature it is generally acknowledged that in an industrial ladle case the desulphurization reaction of liquid steel with slag has a high Pk_o value. So, the steel phase mass transfer is controlled by the steel phase mass transfer resistance. As in Kim & Fruehan (1987), to reproduce the sulphur behaviour within this assumption we have chosen as chemical tracer thymol in the water model. It has a high partition coefficient between oil and water $P > 350$ assuming that k_o is not too small it leads to a water phase mass transfer controlled by the water phase resistance.

Using (3) and (4) we can write that:

$$C'_o = \frac{P\alpha}{1 + \alpha}C_w + \frac{1}{1 + \alpha}C_o \qquad (6)$$

where $\alpha = k_w/Pk_o$. The value of C'_o depends on the magnitude of α. In Kim & Fruehan (1987) it is assumed that $\alpha \ll 1$ giving $C'_o \sim C_o$.

Now if we consider unsteady state, we can write that:

$$\frac{V_w}{A}\frac{dC_w}{dt} = k_w(C_w - C'_w) \qquad (7)$$
$$\frac{V_o}{A}\frac{dC_o}{dt} = k_o(C'_o - C_o)$$

And the mass balance for the transferred species give:

$$(C_{w,0} - C_w)V_w = C_o V_o \qquad (8)$$

Considering the same assumption as in Kim & Fruehan (1987) and equilibrium at the interface it is possible to rewrite (7) using (8) and (4) :

$$\frac{1}{[C_w(1 + \beta) - \beta C_{w,0}]}\frac{dC_w}{dt} = \frac{k_w A}{V_w}$$

where $\beta = V_w/V_o P$. After integration we obtain:

$$\frac{ln\left[\frac{C_w}{C_{w,0}}(1 + \beta) - \beta\right]}{1 + \beta} = \frac{k_w A}{V_w}t \qquad (9)$$

From relation (9), it is possible to compute directly the product of the average mass transfer coefficient with interfacial area per volume unit in function of the measured thymol concentration in water on the left-hand side of (9). This formulation will be used to determine the average mass transfer coefficient in the following experimental results.

Thymol concentration in water is measured every 10 minutes during 3 hours by analysing water samples with a refractometer previously calibrated. Measurements are done with two injection diameters $d_{inj} = 2.35mm$ and $d_{inj} = 7.9mm$, with $14.4l$ of water with a thymol concentration of 0.9g/l dissolved in it and 0.486l of oil mixture atop of it.

NUMERICAL MODEL

To resolve the problem, we solve numerically the partial differential equations with the open-source free code Basilisk. Basilisk is a DNS code with no turbulence model and the possibility to adapt the mesh dynamically following a quad/oc-tree structure. The numerical schemes used in Basilisk are based on its ancestor the Gerris solver and can be found in Popinet (2003), Popinet (2009). The Incompressible Navier-Stokes equations with surface tension term treated by a Continuous Surface Force (Brackbill et al., 1992) can be written:

$$\rho\left(\frac{\partial \boldsymbol{u}}{\partial t} + \boldsymbol{u} \cdot \nabla \boldsymbol{u}\right) = -\nabla p + \nabla \cdot (2\mu \boldsymbol{D})$$
$$+ \sigma\kappa \boldsymbol{n}\delta_s$$
$$\nabla \cdot \boldsymbol{u} = 0$$

with $\boldsymbol{D}$ the deformation tensor $\boldsymbol{D} = (\nabla \boldsymbol{u} + (\nabla \boldsymbol{u})^T)/2$. Because we are dealing with multiphase flow the variations of density and viscosity inside the domain are

described with the help of the Volume Of Fluid method:
The fluid fractions are described by:

$$\chi_k(x,t) = \begin{cases} 1 \ if \ x \ \in phase \ k \\ 0 \ elsewhere \end{cases} \qquad (10)$$

which obeys an advection equation:

$$\frac{\partial \chi}{\partial t} + \boldsymbol{\nabla} \cdot (\chi \boldsymbol{u}) = 0 \qquad (11)$$

Because we are in presence of a three-phase flow, we cannot use the implicit declaration of phase two as in a two-phase flow. Instead, we declare explicitly three fluid fractions corresponding to each phase. To ensure that a cell is not filled with more than one phase the sum of fluid fractions should respect:

$$0 \le \sum_i^n \chi_k(x,t) \le 1 \qquad (12)$$

To do so at each time-step we normalize fluid fractions with the sum of fluid fractions:

$$\chi_{norm}(x,t) = \frac{\chi_k(x,t)}{\sum_i^n \chi_k(x,t)} \qquad (13)$$

This way we can follow a one fluid description with variable density and viscosity determined in the domain with arithmetic means:

$$\rho(\chi) \equiv \chi_a \rho_a + \chi_w \rho_w + \chi_o \rho_o, \qquad (14)$$
$$\mu(\chi) \equiv \chi_a \mu_a + \chi_w \mu_w + \chi_o \mu_o,$$

Surface tension is acting on the interface between two fluids, but here there is more than one possibility of fluid neighbour for one phase. That is why we decompose the physical surface tension into phase-specific surface tension just depending on the phase and not the fluid in contact following K.A. Smith et al. (2002), Chen et al. (2017), Wallmeyer et al. (2018):

$$\sigma_w \equiv (-\sigma_{o/a} + \sigma_{a/w} + \sigma_{w/o})/2 \qquad (15)$$
$$\sigma_o \equiv (\sigma_{o/a} - \sigma_{a/w} + \sigma_{w/o})/2$$
$$\sigma_a \equiv (\sigma_{o/a} + \sigma_{a/w} - \sigma_{w/o})/2$$

To take into account the concentration variation we need to consider also the generic scalar transport equation of concentration c (amount of passive scalar/unit volume) for an incompressible flow and without sources or sinks:

$$\frac{\partial C}{\partial t} = \boldsymbol{\nabla} \cdot (D\boldsymbol{\nabla}C) - \boldsymbol{u} \cdot \boldsymbol{\nabla}C \qquad (16)$$

We can separate (16) in two parts:
- $\boldsymbol{\nabla} \cdot (D\boldsymbol{\nabla}C)$ described the diffusion of C it measures the influence of molecular diffusion on C value;
- $\boldsymbol{u} \cdot \boldsymbol{\nabla}C$ described convection of C on the domain it measures the influence of the flow on C.

It means that C has no influence on the velocity field determined by solving the Navier-Stokes equation and is only used to consider diffusion, therefore we call it a passive scalar or tracer. We define tracers confined to one VOF phase in the same manner as described in López-

Herrera et al. (2015), meaning that tracer cannot cross a VOF interface except through molecular diffusion. This tracer is advected in the flow within the VOF phase to which it is attached. Tracer concentration in a specific phase is given by:

$$T_k = C\chi_k \qquad (17)$$

where C is the amount of chemical species. Because of the formulations used in the Basilisk code, we cannot add easily the equivalent of the partition ratio P at the interface to reproduce the concentration jump. We use instead a Dirichlet condition imposed on the k phase side:

$$if \ \chi_k > 0.5, \qquad T_k' = 0 \qquad (18)$$

Furthermore, to simplify the model we consider constant phase-specific diffusion coefficients with values determined by Sc in water and oil but we set $D_a = 0 \ m^2/s$ in the air phase as we do not consider its influence on the mass transfer.

To have an idea of the smallest scales to be resolved in the simulation we can use the Kolmogorov length scale given by:

$$\eta = \left(\frac{\nu_w^3}{\epsilon/\rho_w} \right)^{1/4} \qquad (19)$$

Pope (2001) postulated that $\Delta \le 2.1\eta$ as a criterion to determine the minimum mesh size needed to resolve the Kolmogorov length scale in a DNS simulation. Now as we are interested to do a simulation of diffusion, the smallest concentration fluctuation scale has been defined as the Batchelor length scale (Batchelor, 1953) and is given by:

$$\lambda_B = \frac{\eta}{Sc^{1/2}} \qquad (20)$$

where $Sc = \mu/\rho D$ is the Schmidt number characterizing the ratio of momentum diffusivity and mass diffusivity. Using Pope criteria with the Batchelor length scale we can determine the minimum number of grid points in one direction required to resolve λ_B:

$$N_B = Sc^{1/2}L_x/(2.1\eta) \qquad (21)$$

Applying this criteria with the water model properties i.e. a Schmidt number of thymol in water of $Sc_{th,w} = 1.48 \ 10^3$ for the highest gas flow rate $Q = 6l/min$ leads to $N_B = 5.21 \ 10^4$ cells. So, to resolve sufficiently the boundary layer, in this case, a maximum resolution of 2^{16} cells in one direction would be necessary. This estimation of mesh resolution might be too strict but gives a worst-case scenario for the simulation. We see that this estimation of mesh resolution leads to a too high mesh resolution to reasonably do a DNS simulation. Instead of that, we do a simulation with smaller Schmidt number. We consider 4 tracers in water with smaller Schmidt numbers in the range of $Sc_{th,w} \in \{1,4,10,40\}$ by adjusting the value of the diffusion coefficient for each tracer. Then from the numerical results, we expect to do a scaling to extrapolate the Sherwood number values to higher Schmidt values. At low value of Schmidt number, the concentration boundary layer thickness is approximately equal to the hydrodynamic boundary layer thickness. If we consider

a maximum mesh resolution in one direction of 2^{10} cells we can describe the oil layer with 26 cells. Now, if we consider an oil droplet of $3mm$ of diameter with the same mesh resolution we end up with 11 cells in its diameter.

RESULTS

EXPERIMENTAL RESULTS

From the evolution of thymol concentration (Figure 2), we can perfectly fit our experimental data at a gas flow rate $Q = 5.5l/min$ with an exponential decay. Taking the slope of the linear fit of the left-hand side of (9) computed from data in Figure 2, we can compute the product of the average mass transfer coefficient with the area. From Figure 3 results the slope of the linear fit is $8.47 \ 10^{-5}$ so it gives here $\overline{k_w}A/V_w = 8.47 \ 10^{-5} \ s^{-1}$.
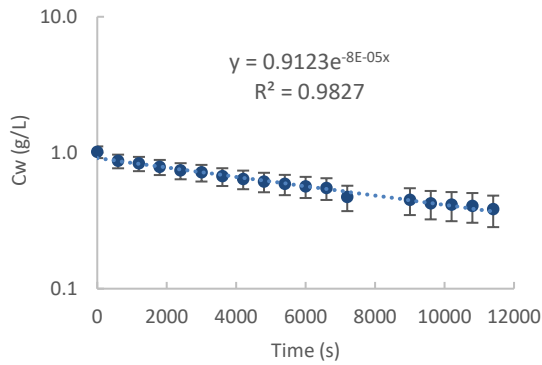

Figure 2: Evolution of thymol concentration for $Q = 5l/min$ and $d_{inj} = 7.9mm$.
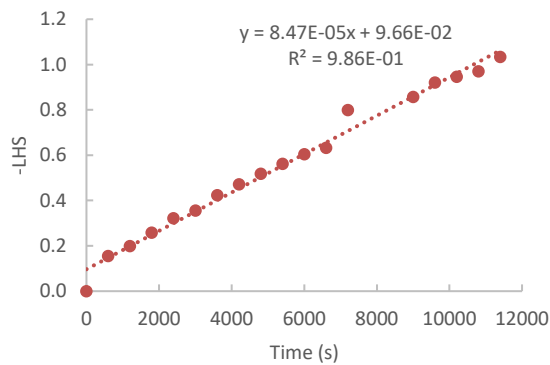
Figure 3: Evolution of - left-hand side of (9) for $Q = 5l/min$ and $d_{inj} = 7.9mm$.

Now, considering the specific water volume for each experiment we can replot the evolution of the product of the mass transfer coefficient with the interfacial area in a log/log scale (Figure 4). From our experimental results (Figure 4) first we can observe that the product of the average mass transfer coefficient with interfacial area increases when the air flow rate is increased for both injection diameters and in agreement with Kim & Fruehan (1987). Even if we have less data for $d_{inj} = 2.35mm$ case it appears that the product of the average mass transfer coefficient with interfacial area varies only a little compared to $d_{inj} = 7.9mm$ results. We can also identify two different mass transfer regimes

below and above a critical air flow rate $Q{\sim}5.0l/min$ for both injection diameters. If we compare the results with the one obtained by Kim & Fruehan (1987), we observe a similar evolution with a critical air flow rate qualitatively the same as the ones we measured with $d_{inj} = 7.9mm$.
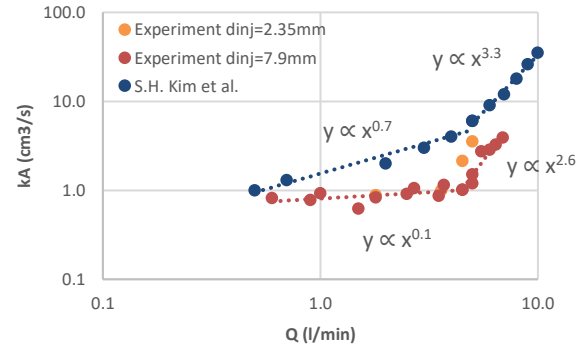
Figure 4: Comparison of the product of the average mass transfer with the interfacial area in function of gas flow rate.

One possible explanation for the mass transfer regime change observed in Figure 4 is the continuous formation of oil droplets of various sizes at high air flow rate. Indeed it can be seen on the top picture of Figure 5 that no oil droplet is visible in water for $Q = 1.0l/min$. As air flow rate increases, we start to see more oil droplets in water only a few minutes after the start of air injection. If we increase air flow rate further, a lot of dark spots which correspond to oil droplets can be identified on the bottom picture of Figure 5 for $Q = 7.5l/min$. Oil droplets of various sizes and shapes are present in water both at the start of air injection and after 3 hours of agitation. These oil droplets could change the interfacial area and the mass transfer mechanism between water and oil droplets.

Figure 5: Front view picture of the experimental model.
Top: $Q = 1.1 l/min$, after 3h of gas stirring.
Bottom: $Q = 7.5 l/min$, after 3h of gas stirring.

NUMERICAL RESULTS

We can see on Figure 6 that the numerical model reproduces globally the same flow behaviour as the one that can be seen on Figure 5. We can identify a central bubble plume generating an oil-free region when it reaches the free surface. The oil layer is relatively stable and no oil droplet is observed at low air flow rate on Figure 5 top picture. On the other hand, the free surface seems to be highly perturbated by gravity waves and possibly reflection from the border of the domain at high air flow rate on Figure 5 bottom picture. We can also note that some oil droplets of various sizes can be identified in the water phase on Figure 5 bottom picture.
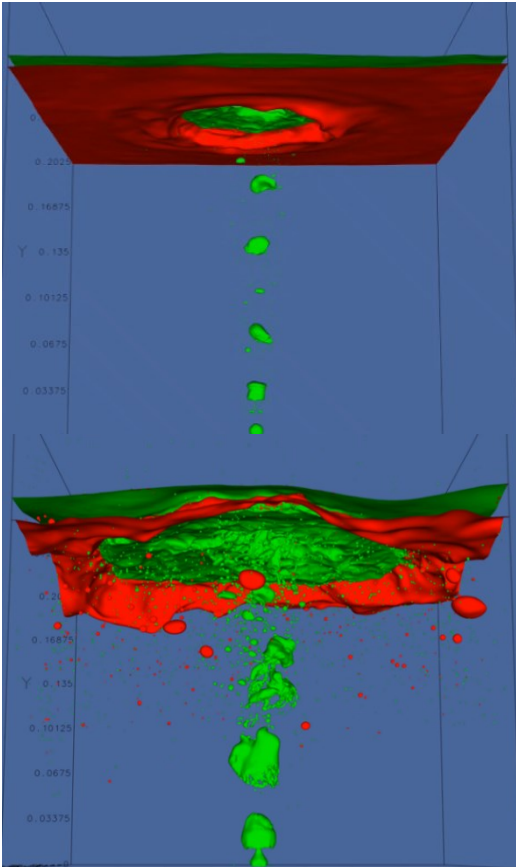
Figure 6: Front view of the numerical model with the air interface coloured in green and the oil interface coloured in red

with a maximum mesh resolution in one direction of 2^9 cells. Top: $Q = 0.6 l/min$; Bottom: $Q = 5.5 l/min.$

We performed simulations for five distinct air flow rates below and around the mass transfer transition observed experimentally. The simulations are started with a maximum mesh resolution in one direction of 2^9 cells. Then when the mass transfer transitory regime is finished, we use the obtained results to restart the simulation with a maximum mesh resolution in one direction increased by a power two. This allows us to save computational time by not recomputing the mass transfer transitory regime for each maximum mesh resolution. From the evolution of the concentration of tracer in water, we can compute the mass transfer coefficient in the water assuming that because of the Dirichlet condition the concentration of tracer at the interface is null. So, we can write:

$$k_w(t)A = \frac{V_w}{C_{w,\infty}} \frac{dC_w}{dt} \qquad (22)$$

As we do not know the experimental oil-water interfacial area, we consider the area without gas injection as reference area $A = L^2$. With this we can compute the average water Sherwood number which is the ratio of convective mass transfer to the rate of diffusive mass transport:

$$Sh_w = \frac{\overline{k_w}}{D_w/h_w} \qquad (23)$$

First, we have to keep in mind that in order to save computational time the numerical results are obtained for a maximum $Sc_{th,w} = 40$ which is thirty seven times lower than the experimental value $Sc_{th,w} = 1.48\,10^3$. From the results of Figure 7, we can see that for a constant flow rate there is a significative gap in the value of the Sherwood number between a maximum mesh resolution in one direction of $lvl9 = 2^9$ cells and higher mesh resolutions. The difference in the Sherwood number value between a maximum mesh resolution in one direction of $lvl10 = 2^{10}$ and $lvl11 = 2^{11}$ cells is small. This indicates that for an air flow rate of $Q = 0.6 l/min$ the results show a mesh convergence for all the Schmidt numbers with a maximum mesh resolution in one direction of $lvl10 = 2^{10}$ cells. We can also note from Figure 7 that the standard deviation increases with the Schmidt number and decreases when the mesh resolution is increased. Looking now at Figure 8 results we can see that either with the experimental results or the numerical results the Sherwood number in water increases when the air flow rate is increased. The experimental results follow the same behaviour than the experimental results of Figure 4 because of the expression of the Sherwood number (23). For the numerical results in the Figure 8, we do not observe abrupt increase of the Sherwood number and so different mass transfer regime.
We can rewrite relation (23) with the Schmidt number:

$$Sh_w = \frac{\overline{k_w}}{v_w/h_w} Sc_w \qquad (24)$$

From (24) we can anticipate that when the diffusion coefficient decreases the Schmidt number increases and so the variation of the concentration of tracer decreases too. For a constant fluid flow, it would lead to a smaller mass transfer coefficient. So, the effect on the value of the Sherwood number depends on the ratio between the decrease of $\overline{k_w}$ and the increases of Sc_w. Now, looking more closely at Figure 8 we can see that when the Schmidt number increases the value of the numerical Sherwood number increases too. This indicates that in our numerical results the increase of the Schmidt number is preponderant over the decrease of the mass transfer coefficient. Furthermore, we can also note that the difference between the experimental and numerical results is more important at low air flow rate than at high air flow rate. And that the numerical results the closer to the experimental results are the ones obtained for $Sc_{th,w} = 40$. Now, if we apply relation (21) at $Q = 5.5 l/min$ with $Sc_{th,w} = 40$ it leads to a necessary maximum mesh resolution of 2^{14} cells in one direction. On the other hand applying (21) at $Q = 0.6 l/min$ with $Sc_{th,w} = 40$ leads to a necessary maximum mesh resolution close to 2^{12} cells in one direction. This indicates that at high Schmidt number the concentration boundary layer is possibly not enough well resolved especially at high air flow rate. If we consider the numerical results at $Q = 0.6 l/min$ as the most converged we can see that there is factor three in the Sherwood number between $Sc_{th,w} = 1$ and $Sc_{th,w} = 10$ but a factor ten between $Sc_{th,w} = 1$ and $Sc_{th,w} = 40$. This indicates that we have to consider with caution the results obtained for $Sc_{th,w} = 40$. The observed overestimation of the Sherwood number especially at high Schmidt number may be due to the usage of a too coarse mesh to represent the concentration boundary layer.
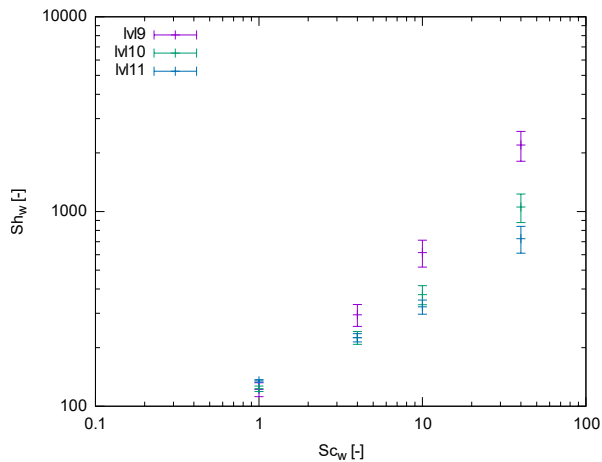
Figure 7: Numerical average water Sherwood number with standard deviation as a function of the Schmidt number in water with different maximum mesh resolution in one direction.
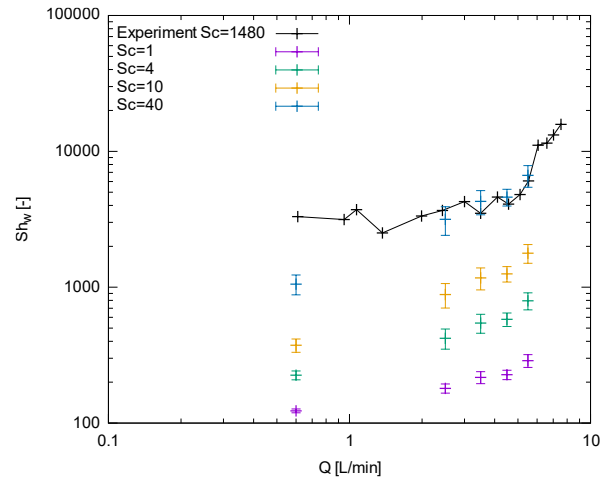
Figure 8: Comparison of experimental (black cross) and numerical average water Sherwood number (colored cross) with standard deviation as a function of gas flow rate. The numerical results are obtained with a maximum mesh resolution in one direction of 2^{10} cells.

CONCLUSION

In this study, we have focused on the mass transfer characterization between water and oil as a model of the industrial process. We have built an experimental model at ambient temperature to reproduce the industrial process. The obtained experimental results show that two different mass transfer regimes of thymol between water and oil phase can be identified in accord with the literature. Furthermore, this change of mass transfer regime seems to be correlated with the continuous formation of oil droplets in water at high air flow rate.

The established numerical model from the experimental water model reproduces qualitatively the same flow behaviour as the one that can be observed in the experimental model. For the mass transfer of the tracer between water and oil we obtained some encouraging results at low Schmidt numbers and for several air flow rates. But the numerical results do not show the abrupt increases of the Sherwood number observed experimentally. Moreover, the numerical results obtained with a much smaller Schmidt number than the experimental one gives similar results than the experimental results. This indicates that the numerical model has a tendency to overestimate the Sherwood number for the high Schmidt number and high air flow rate considered in this study. The fact that numerically no mass transfer regime change is observed may be due to a not sufficiently well described mass transfer around the oil droplets forming at high air flow rate.

REFERENCES

BATCHELOR, G. K. (1953), "The theory of homogeneous turbulence".Cambridge university press.

BRACKBILL, J. U., KOTHE, D. B., & ZEMACH, C. (1992), "A continuum method for modeling surface tension" *Journal of computational physics, ***100**, 335–354.

CALABRESE, R. V., CHANG, T. P., & DANG, P. T. (1986). "Drop breakup in turbulent stirred-tank contactors. Part I: Effect of dispersed-phase viscosity", *AIChE Journal, ***32**, 657–666.

CHEN, X., SUN, Y., XUE, C., YU, Y., & HU, G. (2017), "Tunable structures of compound droplets formed by collision of immiscible microdroplets", *Microfluidics and Nanofluidics, ***21**, 109.

HIRASAWA, M., MORI, K., SANO, M., HATANAKA, A., SHIMATANI, Y., & OKAZAKI, Y. (1987), "Rate of mass transfer between molten slag and metal under gas injection stirring", *Transactions of the Iron and Steel Institute of Japan, ***27**, 277–282.

HIRASAWA, M., MORI, K., SANO, M., SHIMATANI, Y., & OKAZAKI, Y. (1987), "Correlation equations for metal-side mass transfer in a slag-metal reaction system with gas injection stirring", *Transactions of the Iron and Steel Institute of Japan, ***27**, 283–290.

IGUCHI, M., SUMIDA, Y., OKADA, R., & MORITA, Z.-i. (1994), "Evaluation of critical gas flow rate for the entrapment of slag using a water model", *ISIJ international, ***34**, 164–170.

ISHIDA, J. (1981), "Effects of Stirring by Argon Gas Injection on Metallurgical Reactions in Secondary Steelmaking", *Denki-Seiko (Electr. Furn. Steel), ***52**, 2–8.

KIM, S.-H., & FRUEHAN, R. J. (1987), "Physical modeling of liquid/liquid mass transfer in gas stirred ladles", *Metallurgical Transactions B, ***18**, 381–390.

LOPEZ-HERRERA, J. M., GANAN-CALVO, A. M., POPINET, S., & HERRADA, M. A. (2015), "Electrokinetic effects in the breakup of electrified jets: A Volume-Of-Fluid numerical study", *International Journal of Multiphase Flow, ***71**, 14–22.

LOU, W., & ZHU, M. (2014, 10 01), "Numerical Simulation of Desulfurization Behavior in Gas-Stirred Systems Based on Computation Fluid Dynamics–Simultaneous Reaction Model (CFD–SRM) Coupled Model", *Metallurgical and Materials Transactions B, ***45,** 1706–1722.

LOU, W., & ZHU, M. (2015). "Numerical Simulation of Slag-metal Reactions and Desulfurization Efficiency in Gas-stirred Ladles with Different Thermodynamics and Kinetics", *ISIJ International, ***55**, 961-969.

MIETZ, J., SCHNEIDER, S., & OETERS, F. (1991, 1), "Emulsification and mass transfer in ladle", metallurgy. *Steel Research, ***62**, 10–15.

POPE, S. B. (2001), "Turbulent flows". IOP Publishing.

POPINET, S. (2003), "Gerris: a tree-based adaptive solver for the incompressible Euler equations in complex geometries", *Journal of Computational Physics, ***190**, 572-600.

POPINET, S. (2009), "An accurate adaptive solver for surface-tension-driven interfacial flows", *Journal of Computational Physics, ***228**, 5838-5866.

RIBOUD, P., & VASSE, R. (1985), "Désulfuration de l'acier en poche: synthèse des résultats théoriques et industriels", *Revue de métallurgie (Paris), ***82**, 801–810.

SMITH, K. A. (2002), "A projection method for motion of triple junctions by level sets", *Interfaces and Free Boundaries, ***4**, 263-276.

WALLMEYER, B., TRINSCHEK, S., YIGIT, S., THIELE, U., & BETZ, T. (2018), "Collective Cell Migration in Embryogenesis Follows the Laws of Wetting", *Biophysical Journal, ***114**, 213-222.

WEI, T., & OETERS, F. (1992), "A model test for emulsion in gas–stirred ladles", *Steel research, ***63**, 60–68.

XIAO, Z., PENG, Y., & LIU, C. (1987), "Modelling study of the entrapment phenomena at the slag-metal interface in the gas-stirred ladle", *Chinese Journal of Metal Science and Technology, ***3**, 187–193.